Chemical Engineering Journal 494 (2024) 152486

Contents lists available at ScienceDirect

Chemical Engineering Journal

journal homepage: www.elsevier.com/locate/cej

Enhanced separation flux and compressive strength for oil-water separation by adding sodium lignosulphonate

Hui Jiang [a], Jun Li [a,*], Chao Wu [a], Zi-wei Xiong [a], Jia-wei Ding [a], Hui-fen Su [a], Ya-hui Li [a], Wen-bo Luo [a], Liu-jie Yuan [a], Si-yi Lv [a], Lu-xiang Wang [b], De-qiang Li [a]

[a] College of Chemistry and Chemical Engineering, Xinjiang Agricultural University, Urumchi 830052, Xinjiang, PR China
[b] State Key Laboratory of Chemistry and Utilization of Carbon Based Energy Resources, College of Chemistry, Xinjiang University, Urumqi 830017, Xinjiang, PR China

ARTICLE INFO

Keywords:
Sodium lignosulphonate
Graphene oxide
Aerogel
Oil-water separation
Electrostatic interaction
Self-assembly

ABSTRACT

Oil-water separation materials have been deeply developed to solve oil spill problems. However, mechanical strength and separation efficiency remain challenging. Based on the electrostatic repulsion, we design and prepare oil-water separation materials to enhance the separation flux and resistance to pressure by adding sodium lignosulphonate nanoparticles (LSs) to the reduced graphene oxide (rGO), followed by surface modification with trimethoxymethylsilane (MTMS). XRD patterns prove the positive action of LSs for improving interlayer spacing of rGO, which contributes to an excellent separation flux (carbon tetrachloride/water, 43209.71 $L{\cdot}m^{-2}{\cdot}h^{-1}$) of MLNGA. The compressible recovery ability is enhanced to 49.91 kPa under 80 % strain. The MLNGA presents excellent separation efficiency (~99.12 %) on a continuous oil-water separation device. All these results indicate the outstanding performances and potential of MLNGA in oil–water separation applications. Moreover, this design concept involves electrostatic repulsion and may be promoted to other anionic macromolecules such as sodium alginate, tannic acid, and pectin.

1. Introduction

The marine oil spills and discharge of organic pollutants have caused significant harm to the ecological system and the economy. Thus, it is urgent to implement efficient oil-water separation to reduce the resultant environmental pollution and promote resource restoration [1]. The current treatment methods for oil-water mixture contamination include membrane separation [2], centrifugal separation [3], in-situ combustion [4], and oil skimmer [5]. However, efficiency or energy consumption is the bottleneck in the application. Due to their low surface energy and high hydrophobicity, three-dimensional (3D) porous material adsorbents can overcome these disadvantages [6].

Graphene oxide (GO) has been widely employed to form 3D porous materials via the hydrothermal self-assembly method [7], template method [8], chemical crosslinking method, and sol-gel method [9]. The resultant GO-based 3D porous materials are suitable for the adsorption of hydrophilic components due to the abundant oxygen-containing groups on the carbon skeleton, such as carboxyl, hydroxyl, and carbonyl groups. To improve the hydrophobicity, the reduced graphene oxide (rGO) came into being via the hydrothermal method in the presence of reductants. The oxygen-containing functional groups consequently reduce, along with a partial reduction of the sp^2 carbon. This process contributes to the stacking among GO layers, which induces structural collapse [10], viz., the essential interactions for 3D network structure are destroyed, including the π-π conjugation, electrostatic interaction, and hydrogen bonding [11]. Thus, the as-prepared rGO generally presents poor separation flux and compressive strength in oil-water separation. Upholders inserted among the layers can effectively improve the above issues and are added to strengthen the close packing between graphene oxide sheets, such as cellulose [12], double crosslinked networks [13], and metal particles [14]. Deng et al. [14] prepare aerogels from silver phosphate and graphene oxide with significant 3D structures (e.g., specific surface area and pore structure). However, introducing nano-metal particles generally needs suitable functional groups on the metal source, thus showing complexity and challenge [15].

Abbreviations: NGA, EDA/GO aerogel; LNGA, LSs/EDA/GO aerogel; MLNGA, MTMS/LSs/EDA/GO aerogel; MNGA, MTMS /EDA/GO aerogel; GO, Graphene oxide; LSs, Sodium lignosulphonate nanoparticles; EDA, Ethylenediamine; MTMS, Trimethoxymethylsilane.

* Corresponding author.
E-mail address: junli107@163.com (J. Li).

https://doi.org/10.1016/j.cej.2024.152486
Received 30 March 2024; Received in revised form 11 May 2024; Accepted 21 May 2024
Available online 3 June 2024

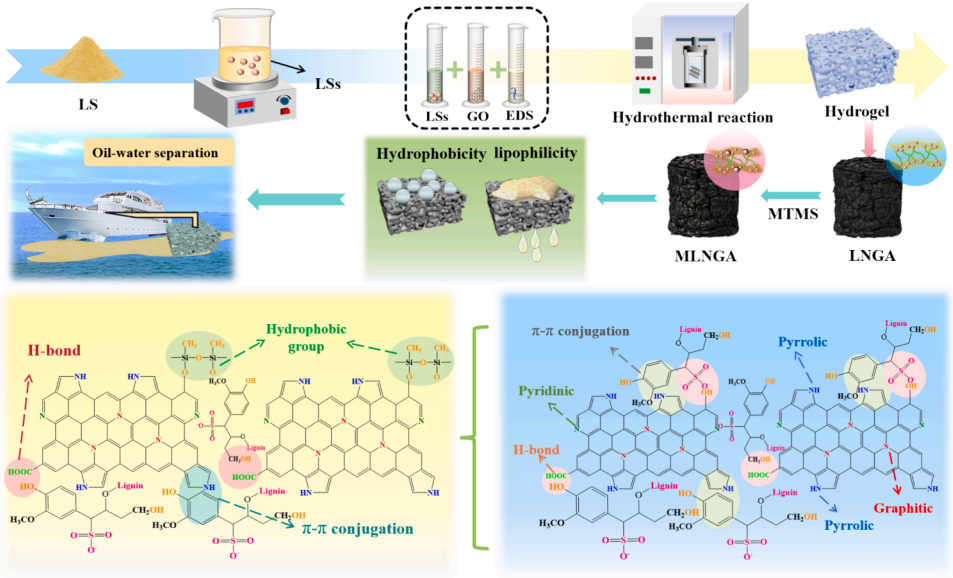

Fig. 1. Schematic of preparation of LNGA and MLNGA.

Natural and synthetic polymers can form nanoparticles to support the rGO layers [16–18]. Thereinto, natural macromolecules have attracted abundant attraction due to their sustainability, low cost, and easy availability. Lignin, a biomacromolecule with a unique aromatic structure, has been one of the most productive natural macromolecules, and 225 million tons of lignin will be produced per year in 2030 because of the incremental requirement of biofuel [19]. It is currently a by-product of the pulping industry, although the "lignin-first" strategy has been proposed for several years. The condensation and electrophilic substitution reactions occur during the cooking process, and the technical lignin accordingly possess a complex chemical structure that limits their high-value utilization. Nevertheless, lignin and lignin derivates contain unique aromatic structures among the natural macromolecules, facilitating physical interactions (e.g., π-π conjugation and hydrogen bonding) with rGO. The phenol unit can also be a reducing agent based on the phenol-quinone conversions. Moreover, the nanoparticle-type lignin improved the mechanical performances of as-prepared biomaterials, such as the strength and elongation at break. Thus, lignin nanoparticles may favor the formation of the 3D pore structure of the resultant rGO-based materials with enhanced mechanical properties.

Yue et al. [20] have prepared aerogels with ultra-lightweight and good mechanical performances from diethylene triamine-functionalized alkali lignin and GO. The electron-rich N atoms can facilely form non-covalent forces with the rGO layer, such as the p-π conjugation and hydrogen bonding. However, these attractions undoubtedly reduce the layer spacing of rGO and the consequent flux in oil-water separation. Sodium lignosulfonate is also a by-product but contains abundant sulfonic acid groups. The existing aromatic rings may endow it to form π-π conjugation with rGO that contributes to preparing bulk; the sulfonic acid groups may support electrostatic repulsion toward rGO layers that favor larger interlamellar spacing and the resultant high separation flux.

The objective of the present study is to verify the role of sodium lignosulfonate based on the abovementioned hypothesis. Thus, sodium lignosulfonate nanoparticles LSs/EDA/GO aerogel (LNGA) are prepared from the LSs and rGO via the hydrothermal method in the presence of ethylenediamine (EDA). The LNGA is further modified by trimethoxymethylsilane to obtain high-hydrophobic bulks (noted as MLNGA). The as-prepared MLNGA shows much higher separation flux and compressive strength than the rGO aerogel and other rGO-based aerogel due to the addition of LSs. We believe this economical, new-type, high-efficiency, and environmentally-friendly oil-water separation material has great potential for oil spill treatment.

2. Materials and methods

2.1. Materials

EDA is provided by Beilian Fine Chemical Development Co., Ltd. (Tianjin, China). MTMS is purchased from Rhawn Chemical Technology Co., Ltd. (Shanghai, China). Sodium lignosulfonate is provided by Damao Chemical Reagent Factory (Tianjin, China). Sodium tripolyphosphate is purchased from Hefei Tianjian Chemical Co., Ltd. (Anhui, China), and graphene oxide is purchased from Suiheng Technology Co., Ltd. (Shenzhen, China).

2.2. Preparation of LSs

The LSs were prepared according to the published data with few modifications [21]. Sodium lignosulfonate is dissolved in deionized water to obtain a suspension with a concentration of 2.4 mg/mL. Then, sodium tripolyphosphate solution with a concentration of 0.8 mg/mL was added to the suspension at a volume ratio of 1:1. The mixture is stirred at a speed of 350 rpm for 15 min and subject to ultrasonic treatment. Then, a suspension of lignin nanoparticles is obtained.

2.3. Preparation of NGA, LNGA, and MLNGA

The GO is dispersed in deionized water for 30 min to obtain a suspension (50 mL, 5 mg/mL), followed by ultrasonic treatment for 45 min. A specific amount of LSs (10 mL) and EDA (0.8 g) is added to the GO suspension and stirred for 1 h. Then, the mixture was transferred into a Teflon-lined hydrothermal reactor to obtain LSs/EDA/GO hydrogel at 200 °C for 24 h. The resultant hydrogel was immersed in deionized water to remove impurities, followed by freeze-drying for 48 h to obtain the LNGA. To address the importance of LSs, we also obey the same route abovementioned to prepare EDA/GO (NGA) without adding LSs.

The hydrophobic modification of LNGA is performed via the coupling reaction in the presence of MTMS. In detail, the LNGA are immersed in 0.4 mL of MTMS in an oven at 105 °C for 10 h. Then, a beaker containing deionized water is placed in the oven once the temperature drops to 60 °C, and the reaction is performed for another 24 h to obtain high hydrophobicity aerogel (referred to as MLNGA). The preparation process of MLNGA is shown in Fig. 1.

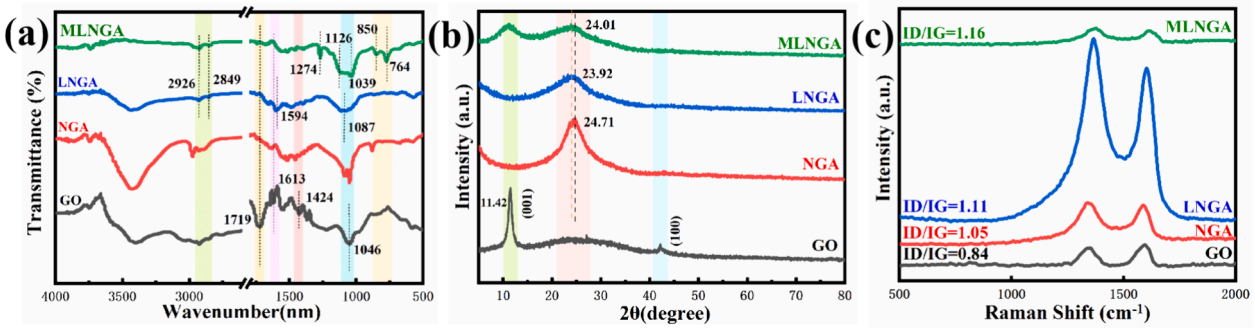

Fig. 2. Physicochemical characteristics of GO, NGA, LNGA, and MLNGA: (a) FTIR spectra, (b) XRD patterns, and (c) Raman spectra.

2.4. Characterization of MLNGA

Fourier transform infrared spectroscopy (FTIR) was used to distinguish the chemical variation of the GO, NGA, LNGA, and MLNGA on a Nicolet iN10 MX spectrometer (Thermo Scientific, USA). D8 Advance X-ray diffractometer (Bruker, Germany) was used to determine the changes in the layer spacing of the prepared materials in the range of 0-80°. The chemical elements in the prepared materials were determined by X-ray photoelectron spectroscopy (XPS, Thermo Scientific, K-Alpha instrument). Raman spectra of the materials were tested with a Raman spectrometer (Raman, LabRAM HR Evolution). The thermogravimetric analyzer (TGA, STA499F3, Netzsch, Germany) was used to determine the thermal stability of the materials in the range of 30-800 °C at a heating rate of 10 °C/min. After spraying gold treatment, the surface microstructure of NGA, LNGA, and MLNGA was scanned by scanning electron microscopy (SEM, JSM-7610Fplus, Japan). The distribution of chemical elements on the surface of MLNGA was investigated by an energy dispersion spectrometer (EDS, INCX-MAX, Japan). Cylindrical aerogel with a gauge of 25 mm and a radius of 22 mm was compressed by a universal tensile and compressive testing machine at a controlled value of 10 mm/min (ZHIQU-990A, China). The water contact angle tester (WCA, SL200B/K, Kono, USA) was used to analyze the wettability of the materials at room temperature.

2.5. Oil-water separation

2.5.1. Determination of adsorption capacity toward oil

The adsorption capacities of MLNGA toward different oils are determined by the immersion method. The MLNGA is immersed in the selected oil until equilibrium adsorption (i.e., saturation) is reached. During this process, the initial weight (W_0) and weight at equilibrium (W_1) of MLNGA are recorded to calculate the adsorption capacity according to the following formula.

$$Q = W_1\text{-}W_0/W_0 \quad (1)$$

In the present study, the adsorption capacities toward oils with different polarity are determined, such as n-hexane, xylene, dichloromethane, chloroform, carbon tetrachloride, soybean oil, rapeseed oil, and dimethyl silicone oil. Each operation is performed in triplicate.

2.5.2. Gravity-driven oil-water separation

This separation system is self-constructed using a funnel, a beaker, and an iron frame. The beaker is placed at the outlet of the funnel and fixed onto the iron frame to collect the separated crude oil. MLNGA is placed at the horn mouth of a 2.0 mm radius glass funnel. The oil-water mixtures are prepared from an equal volume of organic solvents (dichloromethane, chloroform, and carbon tetrachloride) and water, which are subsequently poured into the separator; the time for the oil to drain is recorded to calculate the oil-water separation flux of MLNGA. The separation flux ($L{\cdot}m^{-2}{\cdot}h^{-1}$), viz., permeable volume per unit time, is determined according to Eq. (2).

$$J = V/AT \quad (2)$$

where A (m^2) is the filtration area of the aerogel, i.e., the cross-sectional area of oil passing through aerogel at the funnel in the present study; V (L) denotes the volumes of the collected oil in the beaker, and T (h) is the time required to separate the oil finally. For all the oil-water mixtures, the abovementioned operations are performed ten times to evaluate the material in terms of recycling performance.

2.5.3. Pump-driven oil-water separation

The pump-driven oil-water separation device system consists of a beaker, a vacuum pump, and a suction filter bottle. The vacuum pump and filter bottle are connected with a rubber tube seal, and the MLNGA is fixed at the far end of the vacuum pump. When the pump starts working, the MLNGA is placed into the oil-water mixture that is prepared according to the proportion in 2.5.2. The separation efficiency is evaluated according to Eq. (3).

$$\eta(\%) = (m_2\text{-}m_1)/m_0 \times 100 \quad (3)$$

where m_2 is the total mass of oil-water mixture and beaker, m_1 is the mass of beaker and oil-water mixture after separation, and m_0 is the initial mass of oil.

3. Results and discussion

3.1. Chemical structure analyses of aerogel

FT-IR technique is used to analyze the chemical variability among GO, NGA, LNGA, and MLNGA. In the GO spectrum (Fig. 2a), the typical absorption peaks located at 1719 cm^{-1}, 1424 cm^{-1}, 1613 cm^{-1}, and 1046 cm^{-1} are attributed to the stretching vibrations of C=O, -OH, C=C, and C-O bond [22]. Whereas the peaks at 1719 cm^{-1} disappear in NGA, LNGA, and MLNGA spectra, indicating the reduction reaction during the hydrothermal reaction. Different from the NGA spectrum, the LNGA spectrum shows characteristic peaks at 2926 cm^{-1}, 2846 cm^{-1}, and 1097 cm^{-1} that are ascribed to the stretching vibrations of -OCH_3, -CH_3, and S=O bonds in LSs [23]. The LNGA is further treated by MTMS, and the as-prepared MLNGA appears to have new peaks. Stretching vibration peaks of C-O-Si and O-Si-O linkages can be found at 1126 cm^{-1}, 1039 cm^{-1}, 850 cm^{-1}, and 764 cm^{-1} [24], thereby providing evidence for the silane modification.

The structural changes of different aerogels are compared through X-ray diffraction patterns (Fig. 2b). GO exhibits a distinct characteristic diffraction peak at 11.46°, which can be ascribed to the (0 0 1) crystal plane. This observation indicates that the spacing between adjacent graphene oxide sheets is more significant than that of the original graphite due to the presence of oxygen atoms [25]. Simultaneously, a characteristic diffraction peak corresponding to the (1 0 0) crystal plane appears at 42.25°. The diffraction peak at 11.42° disappears in the XRD pattern of NGA, and the new diffraction peak appears at 24.71°,

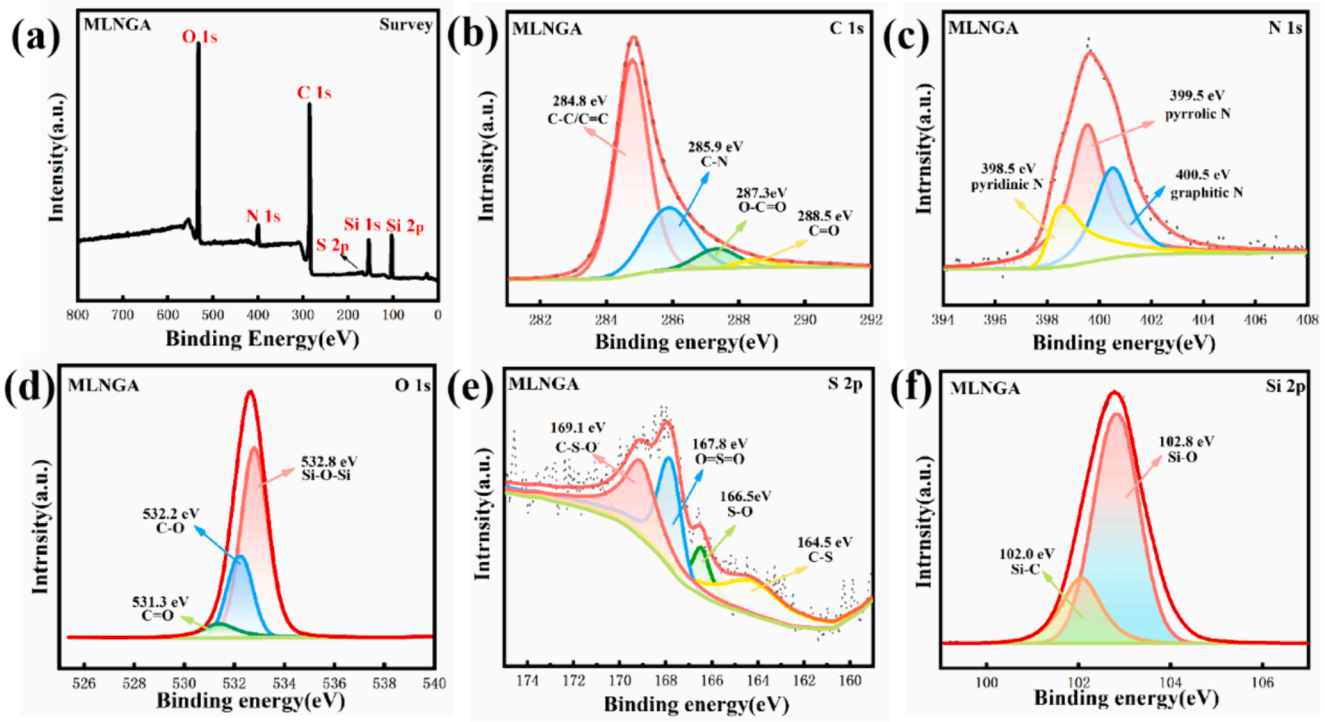

Fig. 3. (a) XPS survey spectra of MLNGA. High-resolution XPS spectra of (b) C 1*s*, (c) N 1*s*, (d) O 1*s*, (e) S 2*p*, and (f) Si 2*p* in MLNGA.

indicating an effective reduction of the oxygen-containing functional group of GO and a decrease in the layer spacing of the rGO. This peak shifts to 23.92° in the XRD pattern of LNGA, indicating the increase in the interlamellar spacing of rGO sheets. According to the $2d\times\sin\theta = n\lambda$, the interlayer spacings of NGA, LNGA, and MLNGA can be calculated as 0.369, 0.380, and 0.379 nm, indicating the positive effect of LSs on increasing interlamellar spacing. These results proved our hypothesis, viz., electrostatic repulsion between LSs and rGO can contribute to the interlamellar spacing that can decrease the fluid resistance in oil/water separation. Moreover, a moderate-intensity peak is found at 10.93°, which contributes to the silicon dioxide [26]. This result proves the successful modification by MTMS, and the consequent interlamellar spacing of MLNGA has shown a slight decrease in LNGA (0.380 nm V.S. 0.379 nm).

Raman spectra for GO, NGA, LNGA, and MLNGA are shown in Fig. 2c. It is evident that there are two classic peaks at 1583 and 1345 cm^{-1} that correspond to the G and D peaks of carbon, respectively. Among them, the G peak represents the plane stretching vibration of sp^2 hybridized carbon atoms, while the D peak represents the defects of the lattice of carbon atoms. The intensity ratio of D peak to G peak (I_D/I_G) is usually used to assess the degree of structural defects, and the increasing ratio indicates the increased structural defects. The I_D/I_G values of GO, NGA, LNGA, and MLNGA are 0.84, 1.05, 1.11, and 1.16, respectively. In comparison, the rGO-contained materials show increased I_D/I_G values, which show the increasing disorder degree caused by the sp^3-hybridized carbon and structural defect, etc. [27]. Moreover, the I_D/I_G value of MLNGA is approximate to that of LNGA, indicating that hydrophobic modification does not enhance the degree of disorder.

3.2. Element composition of MLNGA

XPS analysis aims to characterize the chemical element composition and the surface functional groups of MLNGA. Fig. 3a shows the elemental composition of MLNGA, revealing two obvious characteristic peaks at 532.2 eV and 284.8 eV that correspond to O 1*s* and C 1*s* characteristic peaks. Additionally, MLNGA exhibits N 1*s* and S 2*p* characteristic peaks at 399.5 eV and 167.9 eV, indicating the existence of nitrogen-containing compounds and the successful doping of LSs [28,29]. The appearance of Si 1*s* and Si 2*p* characteristic peaks at 153.2 eV and 102.3 eV further confirm the successful coating reaction of MTMS [17].

The high-resolution XPS spectra of C 1*s*, N 1*s*, O 1*s*, S 2*p*, and Si 2*p* in MLNGA are analyzed to further investigate the elemental composition of MLNGA. The high-resolution spectrum of C 1*s* of MLNGA is shown in Fig. 3b, which exhibits characteristic diffraction peaks corresponding to C-N (286.9 eV), C-C/C=C (284.8 eV), C=O (288.5 eV) and O-C=O (287.8 eV) of MLNGA [30]. Fig. 3c presents the spectrum of N 1*s* in MLNGA, in which the peaks at 405.5 eV, 399.5 eV, and 398.5 eV are ascribed to the existence of graphitic N, pyrrolic N, and pyridinic N [31]. The high-resolution spectra of O 1*s* in MLNGA are depicted in Fig. 3d, where the peaks of C=O, C-O, and Si-O-Si can be found at 531.3 eV, 532.2 eV, and 532.8 eV, respectively [32]. Also, the characteristic diffraction peaks corresponding to C-S-O (169.1 eV), O=S=O (167.8 eV), S-O (166.5 eV), and C-S (164.5 eV) are observed in the S 2*p* spectra (Fig. 3e). Furthermore, the Si-C and Si-O linkages can be identified from the Si 2*p* spectra with the binding energies at 102.0 eV and 102.8 eV (Fig. 3f), these two peaks further prove that MLNGA has been hydrophobically modified. All these results align well with FT-IR analysis.

3.3. Morphology of aerogel

The porous structures of NGA, LNGA, and MLNGA using scanning electron microscopy are shown in Fig. 4. All the aerogels exhibit highly porous microstructures with an ordered orientation. NGA shows a typical rGO structure, i.e., an extensive spacer layer that appears as a smooth parietal layer with obvious fractures (Fig. 4a_1 and 4a_2). Moreover, the thickness of the NGA parietal layer is thinner than that of LNGA and MLNGA (Fig. 4a-4c), dooming that NGA can not have excellent mechanical properties. As a comparison, the LNGA and MLNGA show a well-bedded multilayer structure internally (Fig. 4b and 4c). This phenomenon may be induced by the fact that the LSs disperse among the lamellae, play a role of support inside the aerogel, and further prevent the collapse of the aerogel [33]. In addition, MLNGA shows a significant increase in surface roughness while maintaining its structural integrity

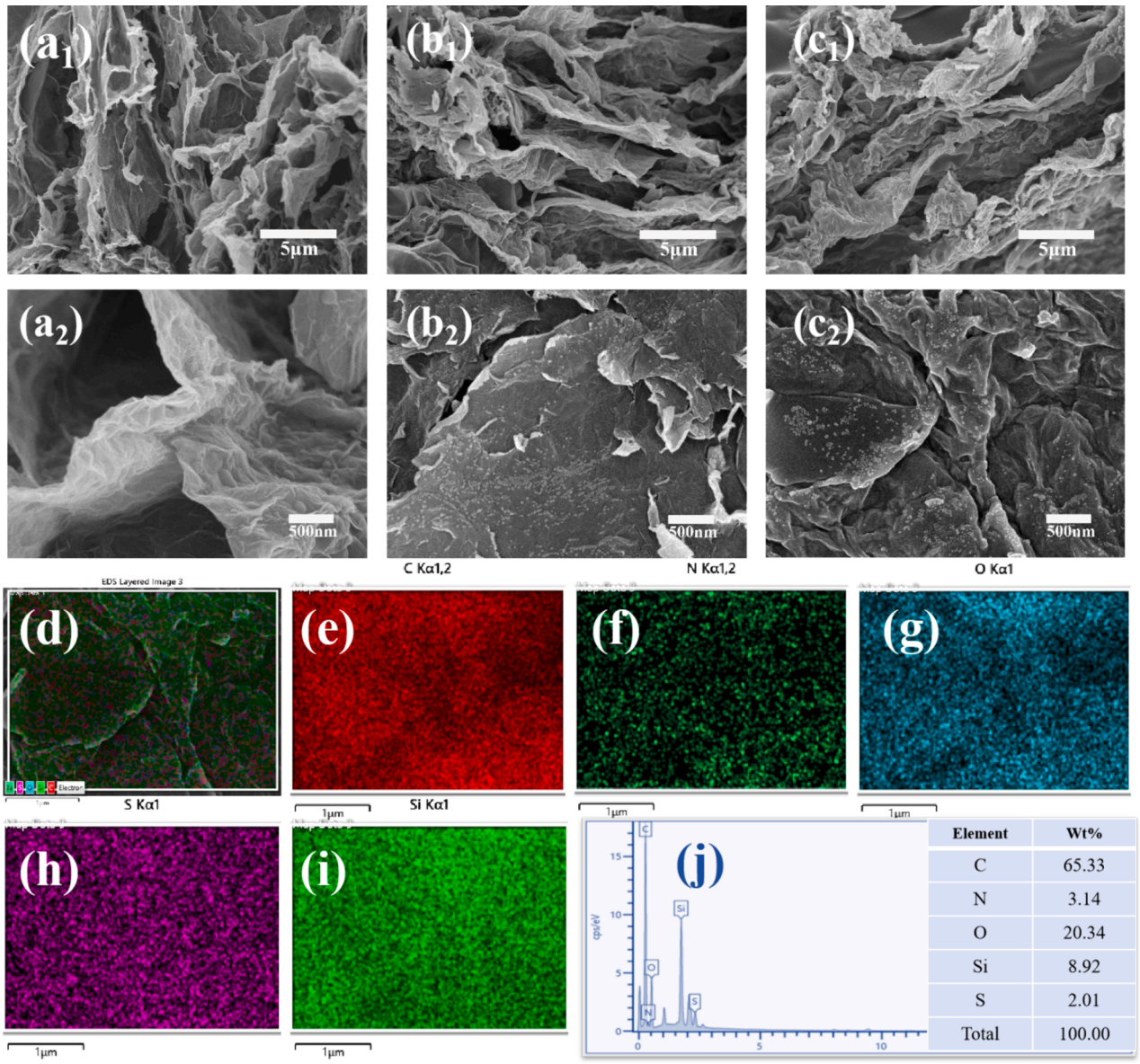

Fig. 4. The morphology of aerogels: SEM images of NGA (a_1-a_2), LNGA (b_1-b_2), and MLNGA (c_1-c_2); (d-i) element mappings of C, N, O, S, and Si of MNGA; (j) EDS spectrum of MLNGA.

(Fig. 4c_1 and 4c_2). The EDS mapping indicates the existence of C, S, O, Si, and N elements (Fig. 4d-4i) with a percentage of 65.33 %, 2.01 %, 20.34 %, 8.92 %, and 3.14 % (Fig. 4j). These results prove that the successful modification by LSs and MTMS.

3.4. Thermal stability and mechanical properties of aerogel

The thermostability of GO, NGA, LNGA, and MLNGA is investigated using the weight loss curves, as presented in Fig. 5a. The initial mass loss below 100 °C can be attributed to the loss of adsorbed water. The unstable oxygen-containing components pyrolyzed in the temperature range of 100-270 °C. Moreover, the thermal weight losses of LNGA and MLNGA are higher than those of NGA in the whole temperature range. This phenomenon may be induced by an increased degree of disorder in rGO, as proved by the Raman spectra. MLNGA has a higher residual quantity than LNGA due to the formation of silicious compounds that act as thermal cracking barriers and effectively prevent damage to the aerogel structure [34].

3.5. Mechanical properties analyses of aerogel

The excellent mechanical properties of aerogels are crucial in oil-water separation, and the results are shown in Fig. 5b-5f. Compressive stress-strain curves show that the stress tolerance under a strain of 30 % of NGA, LNGA, and MLNGA are approximately 2 kPa, 4 kPa, and 4.2 kPa, respectively (Fig. 5b). Thus, the LSs show a positive effect on the mechanical strength. The modification of MTMS does not reduce the mechanical strength of aerogel. Subsequently, compression experiments are conducted on MLNGA under strains of 20 %, 30 %, 40 %, 50 %, 60 %, 70 %, and 80 %, respectively. The corresponding results are presented in Fig. 5c, from which MLNGA can withstand maximum stress of 49.91 kPa under 80 % strain and exhibits sufficient elasticity to restore its shape effectively. Fig. 5d shows that MLNGA demonstrates the ability to recover its original shape even after 50 cycles of compression. All these results indicate that MLNGA possesses excellent mechanical properties and anti-fatigue ability. The flexibility of MLNGA is further confirmed in Fig. 5f_1-f_3 and video S1, from which we can find that the MLNGA can still be restored to its original condition when the 200 g weights are

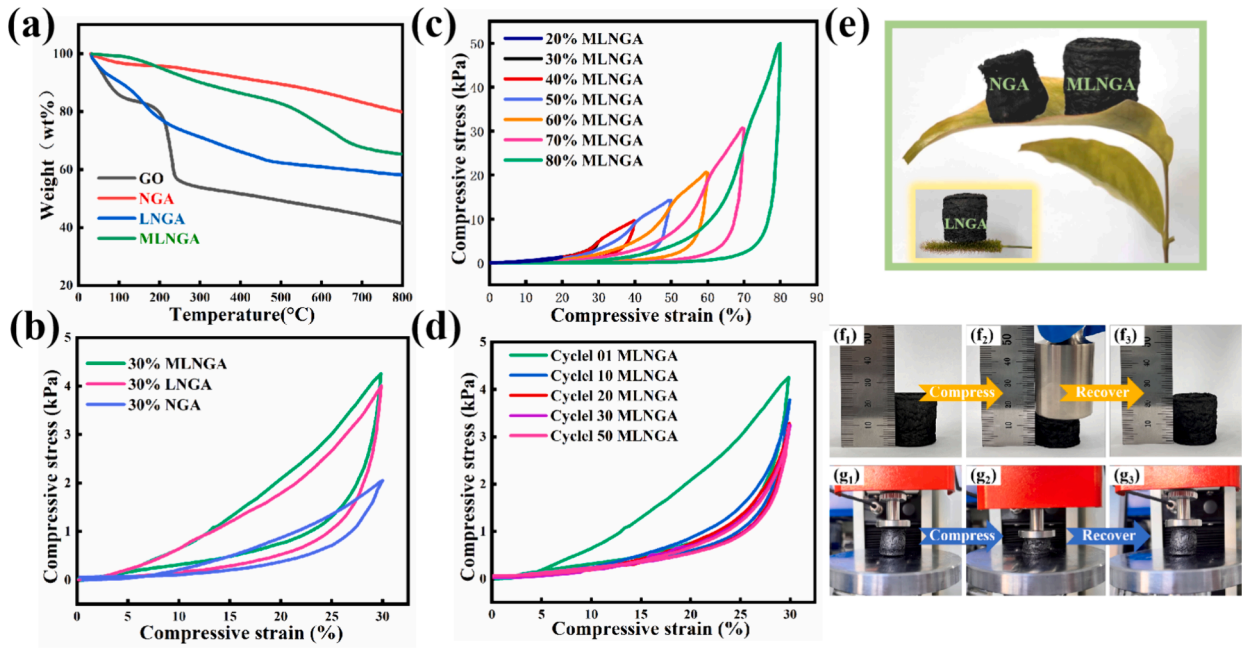

Fig. 5. (a) TGA curves of GO, NGA, LNGA, and MLNGA; (b) compressive stress-strain curves of NGA, LNGA, and MLNGA at 30 % strains; (c) compressive stress-strain curves of MLNGA at 20 %, 30 %, 40 %, 50 %, 60 %, 70 %, and 80 % strains; (d) 50 cycles of compressive stress-strain curve of MLNGA under 30 % strain; (e) macro images of NGA and MLNGA supported by blades and LNGA supported by green bristlegrass; (f_1-f_3) compression experiment of MLNGA under 200 g weight; and (g_1-g_3) 50 cycles of compression experiment of MLNGA under 30 % strain. (For interpretation of the references to colour in this figure legend, the reader is referred to the web version of this article.)

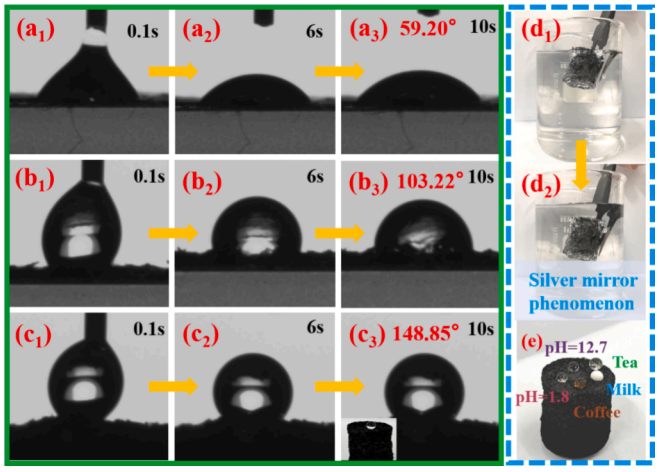

Fig. 6. Wettability of aerogels: water contact angle of (a_1-a_3) NGA, (b_1-b_3) LNGA, and (c_1-c_3) MLNGA; (d_1-d_2) silver mirror phenomenon of MLNGA placed in water; and (e) the image of water, coffee, tea, NaOH aqueous solution with pH=12.7 and HCl aqueous solution with pH=1.8 placed on MLNGA.

removed. As shown in Fig. 5g_1-g_3, MLNGA displays remarkable resilience by recovering nearly its original height even after undergoing 50 cycles of compression at a strain of 30 %. Moreover, the resultant materials have a low density and can be supported on soft leaves or green bristlegrass (Fig. 5e).

3.6. Wettability of aerogel

The wettability of aerogel is the critical condition for the oil-water separation technique. The initial contact angle of NGA is 59.20°, and the water gradually penetrates the pore, indicating a hydrophilic surface (Fig. 6a_1-a_3). As a comparison, the initial contact angle of LNGA increases to 103.22° (Fig. 6b_1-b_3), showing that the LSs can increase the hydrophobicity of the bulk. This phenomenon may be attributed to an increase in the amount of π-π conjugation provided by lignin nanoparticles [35]. These findings indicate that the modification by LSs effectively adjusts the wettability of aerogel. However, it has not yet achieved the high hydrophobicity state, thus necessitating silane modification. The contact angle of MLNGA reaches 148.85°, indicating excellent high hydrophobicity (Fig. 6c_1-c_3) due to the surface coating of methylsilanol groups [36]. When the highly hydrophobic aerogel is forced into the water by an external force, a layer of air forms on its surface, causing refraction and reflection and giving it a good luster. This phenomenon can be found in (Fig. 6d_1-d_2 and video S2), which proves the remarkably high hydrophobicity of the MLNGA. We also drop milk, HCl solution (pH=1.8), coffee, NaOH solution (pH=12.7), and tea on the upper surface of MLNGA, and all the drops show a perfectly spherical shape (Fig. 6e). These results reflect the high hydrophobicity surface that can resist corrosion by acids and bases [37].

Due to the hydrophobicity of MLNGA, we refer to the concept of intrusion pressure formula to further explain the separation mechanism of the oil-water mixture by MLNGA [38].

$$\Delta p = \Delta\gamma/d = C_\gamma(\cos\theta_a)/A \quad (4)$$

where γ is the interfacial tension, d is the diameter of aerogel pores, C is the perimeter of pores, A is the cross-sectional area of pores, and θ_a is the contact angle of liquid on the surface of aerogel. Because the contact angle of water in the air of MLNGA is greater than 90°, the intrusion pressure of water on the surface of aerogel is greater than 0 (i.e., $\Delta p > 0$), which makes it difficult for water to penetrate into aerogel. On the contrary, because of the lipophilicity of MLNGA ($\theta_a < 90°$ and $\Delta p < 0$), oil can penetrate into aerogels.

3.7. Oil-water separation performance

Dichloromethane and n-hexane are mixed with oil red and injected into the water, respectively. The sinking red liquid (i.e., dichloromethane) and floating red liquid (i.e., n-hexane) can be rapidly adsorbed

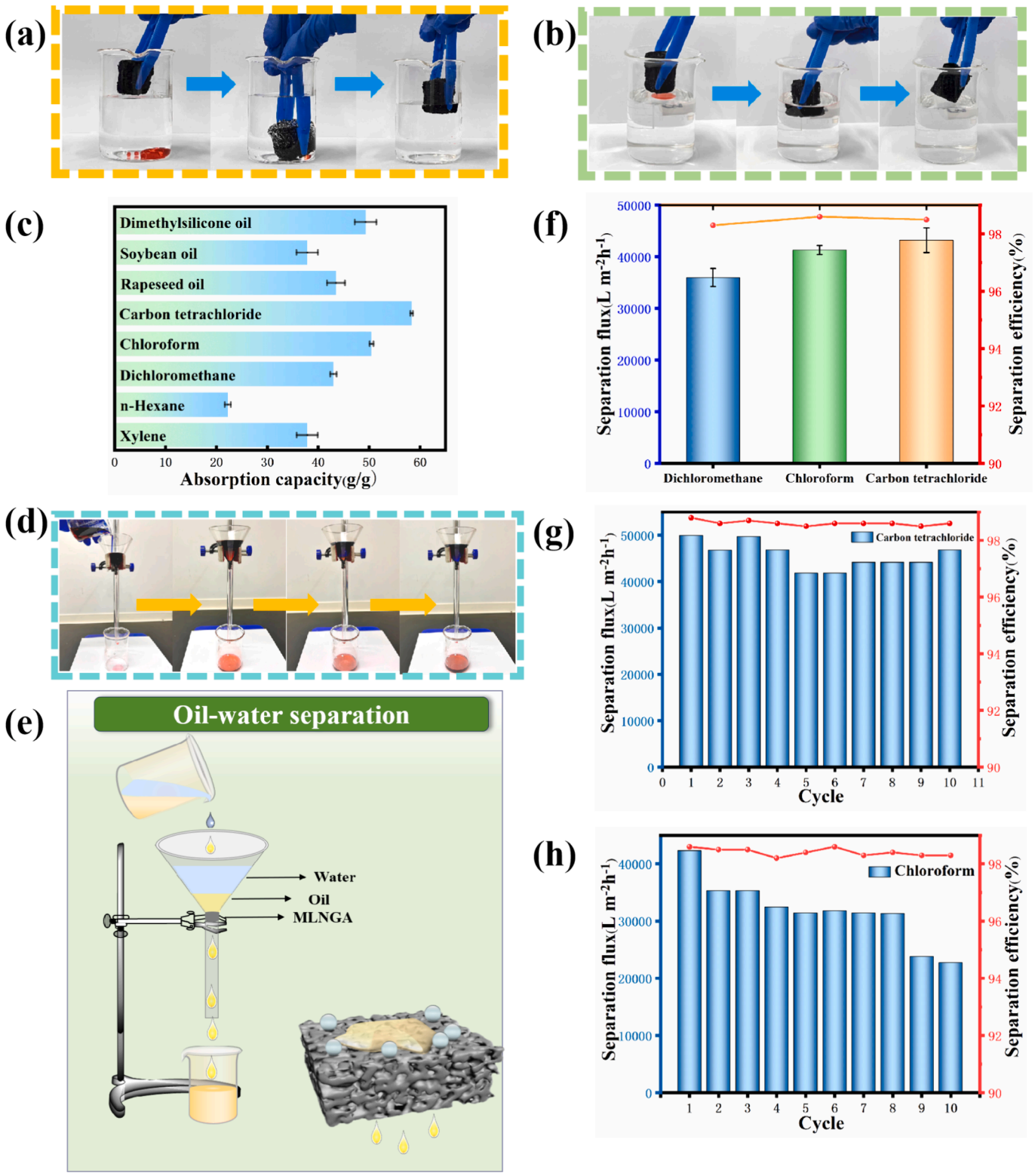

Fig. 7. (a) Image of MLNGA adsorbing dichloromethane in water (oil red staining); (b) image of MLNGA adsorbing n-hexane in water (oil red staining); (c) absorption capacity of MLNGA for xylene, n-hexane, dichloromethane, chloroform, carbon tetrachloride, soybean oil, rapeseed oil, and dimethyl silicone oil; (d) image of MLNGA continuous separation by gravity; (e) schematic diagram of MLNGA continuous separation by gravity; (f) the separation flux and efficiency of MLNGA for dichloromethane, chloroform, and carbon tetrachloride; (g) recovery of carbon tetrachloride by MLNGA after 10 cycles of separation; and (h) recovery of chloroform by MLNGA after 10 cycles of separation. (For interpretation of the references to colour in this figure legend, the reader is referred to the web version of this article.)

Table 1
Comparison between MLNGA aerogel and other reported oil-water separation materials.

Materials	Oil	Flux ($L \cdot m^{-2} \cdot h^{-1}$)	Separation efficiency (%)	Sources
LSs/GO/MTMS	Carbon tetrachloride	43,209	99.12	The present study
SiO_2/PDA	Diesel oil	4000	–	[42]
PC-a/SiO20.6	Chloroform	9300	~90	[43]
PS/CA	Petroleum ether	11,400	~99	[44]
PDMS/PVP	Chloroform	7500	~99	[45]
PVDF/SiO_2/GO	Chloroform	42,402	99.96	[18]

by MLNGA (Fig. 7a-7b and videos S3-S4). Moreover, the MLNGA just adsorbs the low polar solvents and leaves the water phase, indicating its excellent ability of oil-selective adsorption/permeation. The MLNGA can also adsorb dichloromethane from alkaline or acidic mixtures (videos S5-S6), which further reflects that MLNGA has good environmental adaptability. The oil adsorption capacity of MLNGA is further evaluated using solvents with different polar. The absorption capacities of MLNGA to p-xylene, n-hexane, dichloromethane, chloroform, carbon tetrachloride, soybean oil, rapeseed oil, and dimethyl silicone oil are 38, 22, 43, 51, 58, 43, 37, and 49 g/g (Fig. 7c), respectively. These adsorption effects are much better than the other reported materials such as wood/epoxy biocomposite (6-15 g/g) [39], PFS@GC@PDMS (12-27.8 g/g) [40], and MTMS-modified wood aerogel (M-WA) (12.3-25.1 g/g) [41].

A gravity-driven oil-water separation system is employed to determine the separation efficiency of MLNGA (Fig. 7d and video S7). Methylene chloride/water mixture (20 mL, V:V = 1:1) is poured into the glass mouth of the glass funnel. The red oil phase can easily permeate and stream down through the MLNGA while water is trapped above the horn mouth of the funnel (Fig. 7e). This separation effect is achieved by the high hydrophobicity surface of MLNGA. Additionally, the separation fluxes of carbon tetrachloride/water, chloroform/water, and dichloromethane/water mixtures are 43209.71, 41328.44, and 36012.78 $L \cdot m^{-2} \cdot h^{-1}$, respectively. The corresponding efficiencies are 98.35 %, 98.61 %, and 98.57 %, respectively (Fig. 7f).

To further elucidate the excellent performance of MLNGA, we determine the separation fluxes of MNGA, as shown in video S8. However, MNGA is unsuitable for oil-water separation due to its weak mechanical properties and is broken during this process. Moreover, the separation capacity of MLNGA far exceeds that of other materials and has excellent separation efficiency (Table 1). As illustrated in Fig. 7g-7h, MLNGA maintains high separation flux and efficiency even after repeated separation of carbon tetrachloride/water and chloroform/water mixtures 10 times.

As shown in Fig. 8a_1-8a_4 and video S9, MLNGA has excellent mechanical properties and thus can be used for pump-driven oil-water separation. After the device is started, the hexane continuously separates from the mixture without any significant residual oil droplets in the water. The pressure difference between air and oil facilitates the adsorption of oil into the pores of MLNGA (Fig. 8b). Fig. 8c presents that MLNGA exhibits remarkable separation efficiency for n-hexane/water (98.91 %), benzene/water (98.73 %), cyclohexane/water (98.46 %), and xylene/water mixtures (99.12 %). The pump-driven oil-water separation device also confirms the continuous and efficient recovery of oil spills facilitated by the MLNGA. At the same time, we evaluated the stability of MLNGA. After 30 cycles of separation (Fig. S10a), the separation flux of aerogel decreased from 45472.82 $L \cdot m^{-2} \cdot h^{-1}$ to 33862.7 $L \cdot m^{-2} \cdot h^{-1}$. It can be clearly observed that after the tenth adsorption process, the adsorption capacity decreased obviously and then remained relatively stable, indicating that its internal structure was also stable, which was mainly due to the contraction and collapse of the pore structure.

4. Conclusion

We design and prepare MTMS-functionalized LSs/rGO oil/water separation materials. The LSs have been proven to have a positive effect on the interlamellar spacing of rGO, viz., the electrostatic repulsion between LSs and GO may play an important role. Thus, the MLNGA has shown mechanical properties, separation flux, and separation efficiency. The high hydrophobicity surface shows a contact angle of 148.85°, and the compressible recovery ability is also enhanced (49.91 kPa under 80

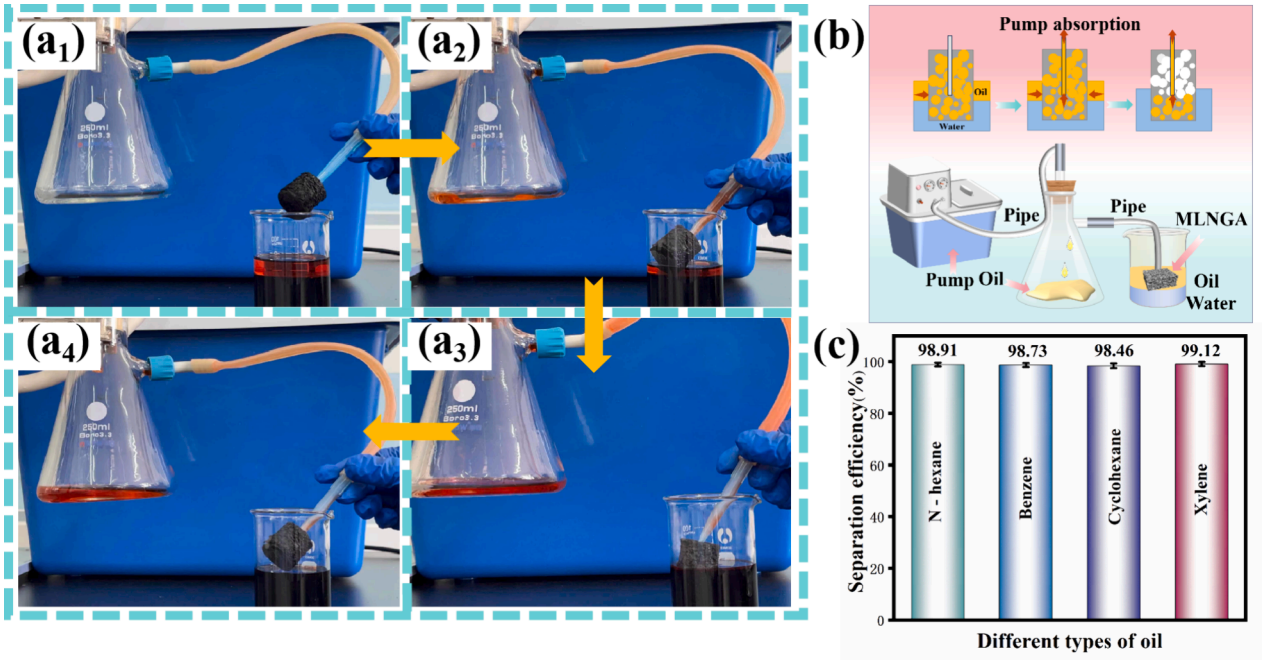

Fig. 8. (a_1-a_4) separation of an oil-water mixture by MLNGA under vacuum pump; (b) schematic diagram of separation of oil-water mixture by MLNGA under the function of vacuum pump; and (c) separation efficiency of benzene, n-hexane, cyclohexane, and xylene by MLNGA.

% strain). The separation flux of MLNGA to carbon tetrachloride/water can achieve 43209.71 $L \cdot m^{-2} \cdot h^{-1}$, and MLNGA remains highly efficient after ten cycles. It also shows excellent separation efficiency (~99.12 %, xylene/water mixtures) on a pump-driven oil-water separation device. All these results indicate the excellent performances and potential of MLNGA in oil-water separation applications.

CRediT authorship contribution statement

Hui Jiang: Writing – original draft, Resources, Methodology, Formal analysis, Data curation, Conceptualization. **Jun Li:** Writing – original draft, Methodology, Investigation, Formal analysis, Data curation, Conceptualization. **Chao Wu:** Visualization, Validation, Supervision, Resources, Methodology, Formal analysis. **Zi-wei Xiong:** Resources, Methodology, Investigation, Formal analysis, Data curation. **Jia-wei Ding:** Writing – original draft, Resources. **Hui-fen Su:** Investigation, Data curation. **Ya-hui Li:** Validation, Investigation, Formal analysis, Data curation. **Wen-bo Luo:** Formal analysis, Data curation. **Liu-jie Yuan:** Formal analysis, Data curation. **Si-yi Lv:** Formal analysis, Data curation. **Lu-xiang Wang:** Visualization, Validation, Supervision, Resources, Methodology, Funding acquisition, Formal analysis. **De-qiang Li:** Writing – original draft, Resources, Methodology, Investigation, Formal analysis, Data curation.

Declaration of competing interest

The authors declare that they have no known competing financial interests or personal relationships that could have appeared to influence the work reported in this paper.

Data availability

Data will be made available on request.

Acknowledgment

The present work is supported by the Natural Science Foundation of Xinjiang Uygur Autonomous Region, China (No. 2022D01A175), The Young Scientific and Technological Innovation Talent, Young Top Talent of Xinjiang, China (No. 2023TSYCCX0039), the Project of Tianshan Innovation Team Plan, China (No. 2023D14020), and Open Project of State Key Laboratory of Chemistry and Utilization of Carbon-based Energy Resources,Xinjiang University, China (NO. KFKT2021001).

Appendix A. Supplementary material

Supplementary data to this article can be found online at https://doi.org/10.1016/j.cej.2024.152486.

References

[1] T. Anselain, E. Heggy, T. Dobbelaere, E. Hanert, Qatar peninsula's vulnerability to oil spills and its implications for the global gas supply, Nat. Sustain. 6 (3) (2023) 273–283, https://doi.org/10.1038/s41893-022-01037-w.
[2] Z. Liu, W. Ma, M. Zhang, Q. Zhang, R. Xiong, C. Huang, Fabrication of superhydrophobic electrospun polyimide nanofibers modified with polydopamine and polytetrafluoroethylene nanoparticles for oil-water separation, J. Appl. Polym. Sci. 136 (24) (2019) 47638. https://doi.org/10.1002/app.47638.
[3] B. Xiang, Q. Sun, Q. Zhong, P. Mu, J. Li, Current research situation and future prospect of superwetting smart oil/water separation materials, J. Mater. Chem. A 10 (38) (2022) 20190–20217, https://doi.org/10.1039/D2TA04469B.
[4] L. Yi, J. Yang, X. Fang, Y. Xia, L. Zhao, H. Wu, S. Guo, Facile fabrication of wood-inspired aerogel from chitosan for efficient removal of oil from water, J. Hazard. Mater. 385 (2020) 121507. https://doi.org/10.1016/j.jhazmat.2019.121507.
[5] X. Zhou, Z. Zhang, X. Xu, X. Men, X. Zhu, Facile fabrication of superhydrophobic sponge with selective absorption and collection of oil from water, Ind. Eng. Chem. Res. 52 (27) (2013) 9411–9416, https://doi.org/10.1021/ie400942t.
[6] Y. Hu, Y. Jiang, L. Ni, Z. Huang, L. Liu, Q. Ke, H. Xu, An elastic MOF/graphene aerogel with high photothermal efficiency for rapid removal of crude oil, J. Hazard. Mater. 443 (2023) 130339. https://doi.org/10.1016/j.jhazmat.2022.130339.
[7] C. Jiang, Z. Wang, J. Li, Z. Sun, Y. Zhang, L. Li, K.-S. Moon, C. Wong, RGO-templated lignin-derived porous carbon materials for renewable high-performance supercapacitors, Electrochim. Acta 353 (2020) 136482. https://doi.org/10.1016/j.electacta.2020.136482.
[8] Z. Dong, L. Zhong, Y. Zhang, F. Liu, H. Huang, Z. Xu, Construction of multifunctional cellulose nanofibers/reduced graphene oxide carbon aerogels by bidirectional freezing for supercapacitor electrodes and strain sensors, Diam. Relat. Mater. 140 (2023) 110555. https://doi.org/10.1016/j.diamond.2023.110555.
[9] J. Huang, D. Li, L. Huang, S. Tan, T. Liu, Bio-based aerogel based on bamboo, waste paper, and reduced graphene oxide for oil/water separation, Langmuir 38 (10) (2022) 3064–3075, https://doi.org/10.1021/acs.langmuir.1c02821.
[10] F. Li, X. Wang, T. Yuan, R. Sun, A lignosulfonate-modified graphene hydrogel with ultrahigh adsorption capacity for Pb(ii) removal, J. Mater. Chem. A 4 (30) (2016) 11888–11896, https://doi.org/10.1039/C6TA03779H.
[11] Q. Fang, Y. Shen, B. Chen, Synthesis, decoration and properties of three-dimensional graphene-based macrostructures: A review, Chem. Eng. J. 264 (2015) 753–771. https://doi.org/10.1016/j.cej.2014.12.001.
[12] C. Li, J. Guo, P. Xu, W. Hu, J. Lv, B. Shi, Z. Zhang, R. Li, Facile preparation of superior compressibility and hydrophobic reduced graphene oxide@cellulose nanocrystals/EPDM composites for highly efficient oil/organic solvent adsorption and enhanced electromagnetic interference shielding, Sep. Purif. Technol. 307 (2023) 122775. https://doi.org/10.1016/j.seppur.2022.122775.
[13] S. Tan, Z. Yang, H. Yuan, J. Zhang, Y. Yang, H. Liu, MnO_2-decorated graphene aerogel with dual-polymer interpenetrating network as an efficient hybrid host for Li-S batteries, J. Alloy. Compd. 791 (2019) 483–489. https://doi.org/10.1016/j.jallcom.2019.03.337.
[14] M. Deng, Y. Huang, RETRACTED: The phenomena and mechanism for the enhanced adsorption and photocatalytic decomposition of organic dyes with Ag_3PO_4/graphene oxide aerogel composites, Ceram. Int. 46 (2) (2020) 2565–2570. https://doi.org/10.1016/j.ceramint.2019.09.128.
[15] C. Chen, X. Zhu, B. Chen, Covalently cross-linked graphene oxide aerogel with stable structure for high-efficiency water purification, Chem. Eng. J. 354 (2018) 896–904. https://doi.org/10.1016/j.cej.2018.08.034.
[16] Y. Yang, Z. Ren, C. Zhou, Y. Lin, L. Shi, L. Hou, Anisotropic superhydrophobic graphene aerogel with radial superelasticity and axial superstiffness for efficient on-demand oil-water separation, J. Mater. Chem. A 11 (36) (2023) 19524–19535, https://doi.org/10.1039/D3TA03859A.
[17] Y.-H. Jiang, Y.-Q. Zhang, C. Gao, Q.-D. An, Z.-Y. Xiao, S.-R. Zhai, Superhydrophobic aerogel membrane with integrated functions of biopolymers for efficient oil/water separation, Sep. Purif. Technol. 282 (2022) 120138. https://doi.org/10.1016/j.seppur.2021.120138.
[18] X. Wang, Z. Liu, X. Liu, Y. Su, J. Wang, T. Fan, X. Ning, S. Ramakrishn, Y.-Z. Long, Ultralight and multifunctional PVDF/SiO_2@GO nanofibrous aerogel for efficient harsh environmental oil-water separation and crude oil absorption, Carbon 193 (2022) 77–87. https://doi.org/10.1016/j.carbon.2022.03.028.
[19] U.S.E.P.A.O.o. Policy, Inventory of US greenhouse gas emissions and sinks: 1990-1994, US Environmental Protection Agency1995.
[20] Y. Yue, Y. Wang, J. Li, W. Cheng, G. Han, T. Lu, C. Huang, Q. Wu, J. Jiang, High strength and ultralight lignin-mediated fire-resistant aerogel for repeated oil/water separation, Carbon 193 (2022) 285–297. https://doi.org/10.1016/j.carbon.2022.03.015.
[21] Y. Jianan, L. Zhaobin, L. Dun, W. Zhuo, L. Jianzhou, Preparation of nanometer sodium lignosulphonate and study on its adsorption of Zn^{2+}, Environ. Prot. Technol. 21 (04) (2015) 21–24, in Chinese.
[22] J. Zhou, Y. Zhang, Y. Yang, Z. Chen, G. Jia, L. Zhang, Silk fibroin-graphene oxide functionalized melamine sponge for efficient oil absorption and oil/water separation, Appl. Surf. Sci. 497 (2019) 143762. https://doi.org/10.1016/j.apsusc.2019.143762.
[23] Z. Li, J. Zhang, L. Qin, Y. Ge, Enhancing antioxidant performance of lignin by enzymatic treatment with laccase, ACS Sustain. Chem. Eng. 6 (2) (2018) 2591–2595, https://doi.org/10.1021/acssuschemeng.7b04070.
[24] X. Zhang, H. Wang, Z. Cai, N. Yan, M. Liu, Y. Yu, Highly compressible and hydrophobic anisotropic aerogels for selective oil/organic solvent absorption, ACS Sustain. Chem. Eng. 7 (1) (2019) 332–340, https://doi.org/10.1021/acssuschemeng.8b03554.
[25] Y. He, F. Wu, X. Sun, R. Li, Y. Guo, C. Li, L. Zhang, F. Xing, W. Wang, J. Gao, Factors that affect pickering emulsions stabilized by graphene oxide, ACS Appl. Mater. Interfaces 5 (11) (2013) 4843–4855, https://doi.org/10.1021/am400582n.
[26] L. Liu, G. Kong, Y. Zhu, D. Lai, S. Zhang, C. Che, Ultralight, compressive and superhydrophobic methyltriethoxysilane-modified graphene aerogels for recyclable and selective organic pollutants adsorption from water, Appl. Surf. Sci. 598 (2022) 153694. https://doi.org/10.1016/j.apsusc.2022.153694.
[27] W. Ye, X. Li, J. Luo, X. Wang, R. Sun, Lignin as a green reductant and morphology directing agent in the fabrication of 3D graphene-based composites for high-performance supercapacitors, Ind. Crop. Prod. 109 (2017) 410–419. https://doi.org/10.1016/j.indcrop.2017.08.047.
[28] Y. Wang, X. Hu, Y. Liu, Y. Li, T. Lan, C. Wang, Y. Liu, D. Yuan, X. Cao, H. He, L. Zhou, Z. Liu, J.W. Chew, Assembly of three-dimensional ultralight poly (amidoxime)/graphene oxide nanoribbons aerogel for efficient removal of uranium (VI) from water samples, Sci. Total Environ. 765 (2021) 142686. https://doi.org/10.1016/j.scitotenv.2020.142686.
[29] M. Yan, W. Huang, Z. Li, Chitosan cross-linked graphene oxide/lignosulfonate composite aerogel for enhanced adsorption of methylene blue in water, Int. J. Biol. Macromol. 136 (2019) 927–935. https://doi.org/10.1016/j.ijbiomac.2019.06.144.
[30] H. Li, P. Zang, H. Liu, J. Li, B. Zhang, C. Yu, Y. Jiao, H. Li, Fabrication and electrochemical behavior of halloysite/graphene-polyaniline three-dimensional

hybrid aerogel loaded with iron oxide, J. Alloy. Compd. 871 (2021) 159157. https://doi.org/10.1016/j.jallcom.2021.159157.
[31] H.-B. Zhao, W.-D. Wang, Q.-F. Lü, T.-T. Lin, Q. Lin, H. Yang, Preparation and application of porous nitrogen-doped graphene obtained by co-pyrolysis of lignosulfonate and graphene oxide, Bioresour. Technol. 176 (2015) 106–111. https://doi.org/10.1016/j.biortech.2014.11.035.
[32] Z. Wan, R. Shu, J. Zhang, Y. Wu, Synthesis of three-dimensional porous nitrogen-doped reduced graphene oxide/multi-walled carbon nanotubes composite aerogel as lightweight and high-performance electromagnetic wave absorbers, Diam. Relat. Mater. 112 (2021) 108245. https://doi.org/10.1016/j.diamond.2021.108245.
[33] H. Zhang, X. Zhang, L. Wang, B. Wang, X. Zeng, B. Ren, X. Yang, Synthesis of a lignin-enhanced graphene aerogel for lipase immobilization, ACS Omega 8 (2) (2023) 2435–2444, https://doi.org/10.1021/acsomega.2c06908.
[34] A. Jamsaz, E.K. Goharshadi, Flame retardant, superhydrophobic, and superoleophilic reduced graphene oxide/orthoaminophenol polyurethane sponge for efficient oil/water separation, J. Mol. Liq. 307 (2020) 112979. https://doi.org/10.1016/j.molliq.2020.112979.
[35] H. Sun, Z. Liu, K. Liu, M.E. Gibril, F. Kong, S. Wang, Lignin-based superhydrophobic melamine resin sponges and their application in oil/water separation, Ind. Crop. Prod. 170 (2021) 113798. https://doi.org/10.1016/j.indcrop.2021.113798.
[36] Y. Yi, P. Liu, N. Zhang, M.E. Gibril, F. Kong, S. Wang, A high lignin-content, ultralight, and hydrophobic aerogel for oil-water separation: preparation and characterization, J. Porous Mater. 28 (6) (2021) 1881–1894, https://doi.org/10.1007/s10934-021-01129-6.
[37] Y. Meng, F. Song, H. Chen, Y. Cheng, J. Lu, H. Wang, Composited gels from nature growing scaffold: synthesis, properties, and application, ACS Appl. Mater. Interfaces 13 (4) (2021) 5498–5507, https://doi.org/10.1021/acsami.0c18504.
[38] Q.-M. Wang, J.-C. Lin, Z.-H. Liu, Q.-F. Lü, Covalently grafted amino acid-modified $Ti_3C_2T_x$ to construct an interface for separation of oily wastewater and dye wastewater, Ceram. Int. 49 (11, Part A) (2023) 17437–17452. https://doi.org/10.1016/j.ceramint.2023.02.112.
[39] Q. Fu, F. Ansari, Q. Zhou, L.A. Berglund, Wood nanotechnology for strong, mesoporous, and hydrophobic biocomposites for selective separation of oil/water mixtures, ACS Nano 12 (3) (2018) 2222–2230, https://doi.org/10.1021/acsnano.8b00005.
[40] Z. Liu, M. Chen, C. Lin, F. Li, J.T. Aladejana, J. Hong, G. Zhao, Z. Qin, X. Zhu, W. Zhang, D. Chen, X. Peng, T. Chen, Solar-assisted high-efficient cleanup of viscous crude oil spill using an ink-modified plant fiber sponge, J. Hazard. Mater. 432 (2022) 128740. https://doi.org/10.1016/j.jhazmat.2022.128740.
[41] Y. Zhu, H. Li, W. Huang, X. Lai, X. Zeng, Facile fabrication of superhydrophobic wood aerogel by vapor deposition method for oil-water separation, Surf. Interfaces 37 (2023) 102746. https://doi.org/10.1016/j.surfin.2023.102746.
[42] F. Guo, Q. Wen, Y. Peng, Z. Guo, Simple one-pot approach toward robust and boiling-water resistant superhydrophobic cotton fabric and the application in oil/water separation, J. Mater. Chem. A 5 (41) (2017) 21866–21874, https://doi.org/10.1039/C7TA05599D.
[43] H. Yao, X. Lu, Z. Xin, H. Zhang, X. Li, A durable bio-based polybenzoxazine/SiO_2 modified fabric with superhydrophobicity and superoleophilicity for oil/water separation, Sep. Purif. Technol. 229 (2019) 115792. https://doi.org/10.1016/j.seppur.2019.115792.
[44] C. Xiong, Z. Quan, H. Zhang, L. Wang, X. Qin, R. Wang, J. Yu, Hierarchically tunable structure of polystyrene-based microfiber membranes for separation and selective adsorption of oil-water, Appl. Surf. Sci. 532 (2020) 147400. https://doi.org/10.1016/j.apsusc.2020.147400.
[45] H. Guo, J. Yang, T. Xu, W. Zhao, J. Zhang, Y. Zhu, C. Wen, Q. Li, X. Sui, L. Zhang, A robust cotton textile-based material for high-flux oil-water separation, ACS Appl. Mater. Interfaces 11 (14) (2019) 13704–13713, https://doi.org/10.1021/acsami.9b01108.